Thermolysis of Noble Metal Nanoparticles into Electron-Rich Phosphorus-Coordinated Noble Metal Single Atoms at Low Temperature

Peng Zhou, Ning Li, Yuguang Chao, Weiyu Zhang, Fan Lv, Kai Wang, Wenxiu Yang, Peng Gao, and Shaojun Guo*

Abstract: *Noble metal single atoms coordinated with highly electronegative atoms, especially N and O, often suffer from an electron-deficient state or poor stability, greatly limiting their wide application in the field of catalysis. Herein we demonstrate a new PH_3-promoted strategy for the effective transformation of noble metal nanoparticles (MNPs, M = Ru, Rh, Pd) at a low temperature (400°C) into a class of thermally stabilized phosphorus-coordinated metal single atoms (MPSAs) on g-C_3N_4 nanosheets via the strong Lewis acid–base interaction between PH_3 and the noble metal. Experimental work along with theoretical simulations confirm that the obtained Pd single atoms supported on g-C_3N_4 nanosheets exist in the form of PdP_2 with a novel electron-rich feature, conceptionally different from the well-known single atoms with an electron-deficient state. As a result of this new electronic property, PdP_2-loaded g-C_3N_4 nanosheets exhibit 4 times higher photocatalytic H_2 production activity than the state-of-art N-coordinated PdSAs supported on g-C_3N_4 nanosheets. This enhanced photocatalytic activity of phosphorus-coordinated metal single atoms with an electron-rich state was quite general, and also observed for other active noble metal single atom catalysts, such as Ru and Rh.*

Recently, metal single-atom (MSA) catalysts with nearly 100% atomic utilization efficiency and unique catalytic properties have received wide attention in the fields of electrocatalysis, thermocatalysis, and photocatalysis.[1] However, the undesirable aggregation of MSAs, owing to their high surface energy, often reduces the number of the catalytically active centers or even deactivates the catalyst.[1f,2] In general, the aggregation of MSAs is typically attributed to the migration of atomic metal species due to weak metal–support interactions or strong metal–metal interaction.[3] Introducing suitable ligands to the surface of the support to stabilize MSAs is an effective approach to enhance the metal–support interactions, which can inhibit the migration tendency of noble metal SAs.[4]

Various ligand strategies have been proposed to enhance the metal–support interactions. However, some common ligand atoms, such as N, O, and S, have high electronegativity, which easily leads to the coordinated MSAs that are highly oxidized.[5] For some catalytic reactions the electronic state of the catalytic centers probably determines the reactant adsorption, activation, formation of intermediate, and product desorption.[3d,4a,c,6] Especially for catalytic reduction reactions, an electron-rich center is beneficial to the reduction of reactant.[4c,6b,7] However, the high-electronegativity ligands probably poison or deactivate the MSA centers, which thus limits their application in catalysis. Besides, the coordination between those high-electronegativity ligand atoms and MSAs often requires high temperatures (> 900°C), which easily destroy the support, especially photocatalyst semiconductors.[8]

Hence, some low-electronegativity atoms are potential ligand candidates for constructing the electron-rich MSA centers with optimized electronic properties and chemical activity, which is particularly attractive for catalysis. Here, we develop a PH_3-assisted strategy to transform metal (M = Ru, Rh, Pd) nanoparticles (MNPs) into thermally stabilized phosphorus-coordinated metal single atoms (MPSAs) on g-C_3N_4 (CN) at a low temperature of 400°C. Experimental and theoretical methods were used to study the formation process and the electronic and catalytic properties of phosphorus-coordinated MSAs. The photocatalytic H_2 production was studied to understand the effect of phosphorus coordination on the catalytic properties of MSAs. The results reveal that PdP_2-loaded g-C_3N_4 nanosheets with new electronic property can have 4 times higher photocatalytic activity for H_2 production than the state-of-art N-coordinated PdSAs supported on g-C_3N_4 nanosheets.

The crystalline Pd nanoparticles (NPs) were first loaded on g-C_3N_4 by the photoreduction method, and then heated at 400°C under an N_2 atmosphere (Figure 1a) (denoted as PdNP-CN). After that, PdNP-CN was heated to 400°C in the presence of NaH_2PO_2. In this process, NaH_2PO_2 was decom-

[*] P. Zhou, Y. Chao, W. Zhang, F. Lv, K. Wang, W. Yang, Prof. S. Guo
Department of Materials Science and Engineering
Peking University, Beijing 100871 (China)
and
Beijing Innovation Center for Engineering Science and Advanced Technology, Peking University, Beijing 100871 (China)
and
Key Laboratory of Theory and Technology of Advanced Batteries Materials, College of Engineering
Peking University, Beijing 100871 (China)
E-mail: guosj@pku.edu.cn

N. Li, Prof. P. Gao
Electron Microscopy Laboratory and International Center for Quantum Materials, School of Physics
Peking University, Beijing 100871 (China)
and
Academy for Advanced Interdisciplinary Studies
Peking University, Beijing 100871 (China)
and
Collaborative Innovation Centre of Quantum Matter
Beijing 100871 (China)

📄 Supporting information and the ORCID identification number(s) for
ⓘ the author(s) of this article can be found under:
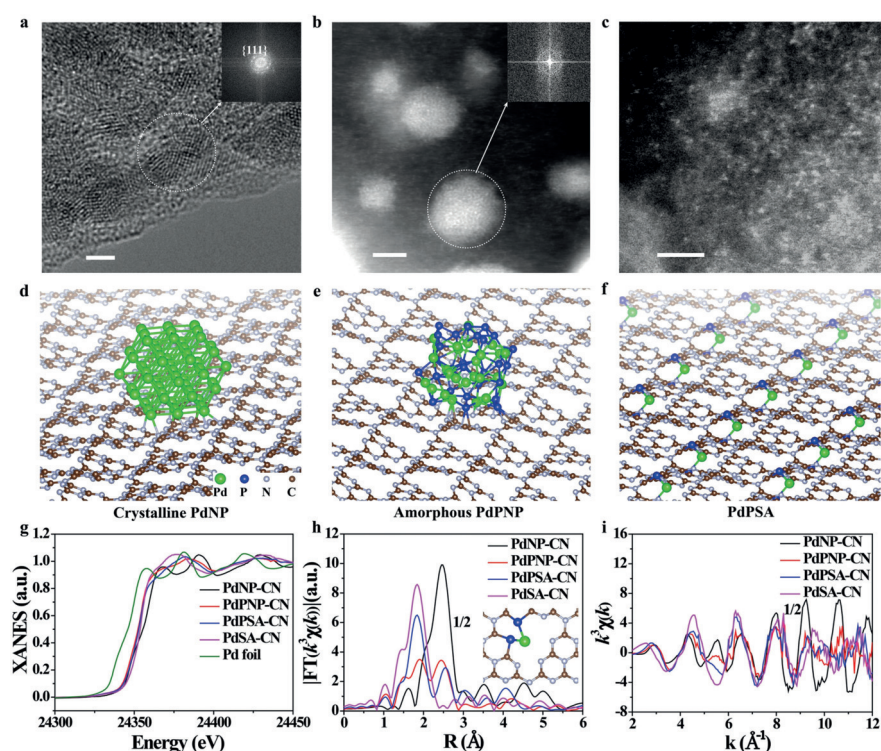https://doi.org/10.1002/anie.201908351.

Figure 1. a) HRTEM image of PdNP-CN. HAADF-STEM images of b) PdPNP-CN and c) PdPSA-CN. The geometry structures of d) PdNP-CN, e) PdPNP-CN, and f) PdPSA-CN. g) Pd K-edge XANES spectra and the corresponding k^3-weighted FT spectra at h) R and i) k space. Scale bar: 2 nm.

6.31 $Å^{-1}$ in PdPSA-CN is also assigned to the Pd–P bonds. To determine the quantitative chemical configuration of Pd atom, the EXAFS fitting was performed to extract the structure parameters (Figures S2 and S3). The centered Pd atoms in the as-prepared samples have two coordinating interactions: Pd–P and Pd–Pd (Table S2). In the first phosphatizing treatment, the coordination number of Pd–Pd changes from 8.01 to 2.10. Meanwhile, partial Pd–P and Pd–N bonds also form in PdPNP-CN. However, the total coordination number of the Pd centers is lower than 3.7, implying its high degree of unsaturation. Thus it is not strange that the Pd nanoparticles are amorphous in PdPNP-CN (Figure 1b). With further phosphatization, the coordination number of Pd–Pd decreased to approximately 1.31 and the coordination number of Pd–P increased to 2.22. The low coordination number of Pd implies atomically dispersed Pd atoms, while the Pd–Pd bond is attributed to the sub-nanometer-sized Pd clusters. According to these results, it is concluded that the present phosphatizing treatments can transform PdNPs into P-coordinated Pd single atoms (PdPSAs) on g-C_3N_4.

posed into PH_3, which reacted with PdNPs. The obtained sample was denoted as PdPNP-CN. The high-resolution high-angle annular dark-field scanning transmission electron microscopy (HAADF-STEM) image shows that the crystalline PdNPs were converted into amorphous nanoparticles without lattice fringes (Figure 1b). Interestingly, when PdPNP-CN was further phosphatized, numerous Pd single atoms and slight nanoclusters were formed on g-C_3N_4 (Figure 1c and Figure S1). To exclude the possibility of PdNPs loss instead of the transformation of PdNPs to PdPSAs, the Pd content of the as-prepared samples was measured by inductively coupled plasma optical emission spectrometry (ICP-OES), which showed that Pd still remained in the PH_3-treated samples (Table S1).

To illustrate the structure evolution of the Pd species in the phosphatizing treatments (Figure 1d–f), and further confirm the atomical dispersion of Pd species in PdPSA-CN, X-ray absorption near-edge structure (XANES) and extended X-ray absorption fine structure (EXAFS) measurements were performed to study the coordination of Pd. XANES data shows that the K-edge absorption line of PdPNP-CN and PdPSA-CN is lower than that of PdNP-CN, implying the lower degree of oxidation of Pd in PdPNP-CN and PdPSA-CN (Figure 1g). The EXAFS results reveal one dominant peak at around 1.8 Å in PdPSA-CN, attributed to Pd–P bonds, while the peak at around 2.45 Å in PdNP-CN corresponds to the Pd–Pd bonds in PdNPs (Figure 1h). The wavelet transform (WT) was used to further analyze the Pd K-edge EXAFS oscillations (Figure 1i). The WT maximum at

Similarly, the MNP-to-MPSA transformation was also observed for Ru and Rh metals. Here, too, the crystalline RuNPs and RhNPs were first transformed into amorphous nanoparticles (intermediate state) with the assistance of PH_3 at 400°C (Figures S4 and S5). Then further phosphatizing treatments directly converted the amorphous nanoparticles into the MSAs (Figure 2a,b, and Figures S6 and S7). The XANES results confirm the higher reduction degree of the Ru/Rh species in Ru/RhPSA-CN compared to that in Ru/RhNP-CN (Figure S8). The EXAFS and WT data also suggest that the Ru/Rh–P bonds are dominant in Ru/RhPSA-CN (Figure 2c,d and Figure S9). The corresponding fitting results show that the Ru/Rh centers tend to be coordinated to around four P atoms and one Ru/Rh atom on average (Figures S10–S13, Tables S3 and S4). These results strongly indicate that MNP-to-MPSA transformation is not limited to Pd but is a common pathway to dissociate NPs into SAs with an amorphous structure as the intermediate state.

As a comparison, common N/O-coordinated metal SAs (MSAs) were also synthesized on g-C_3N_4 (denoted as MSA-CN) by a reported icing-assisted photocatalytic reduction method.[3d] The XANES results show that MSA-CN is at a more highly oxidized than MPSA-CN (Figure 1g and Figure S8). The EXAFS and the corresponding fitting results also confirm the existence of atomically dispersed metal species (Tables S3 and S4). Besides, the Ru/Rh/Pd–N bonds in Ru/Rh/PdSA-CN are shorter than the Ru/Rh/Pd-P bonds in Ru/Rh/PdPSA-CN, confirmed by the EXAFS fittings and
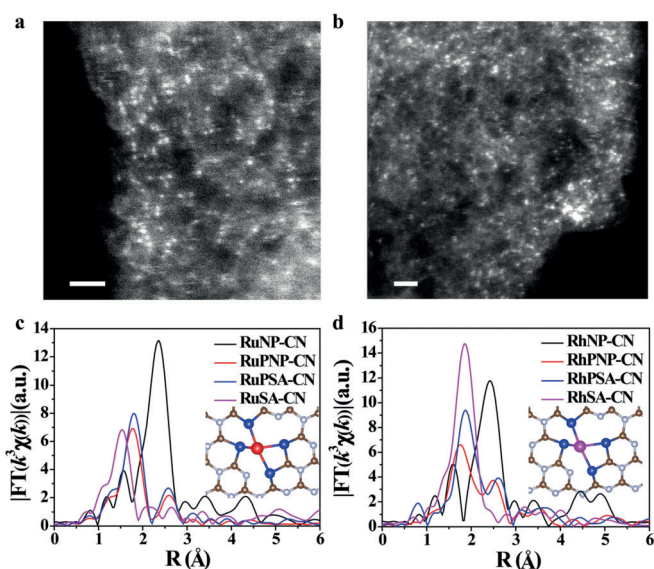
Figure 2. HAADF-STEM images of a) RuPSA-CN and b) RhPSA-CN. EXAFS spectra of c) Ru and d) Rh at R space. Scale bar: 1 nm.

DFT simulations (Tables S3–S5). These results confirm the advantage of the present strategy in preparing the highly reduced metal SAs.

Herein, X-ray diffraction (XRD) patterns of all as-prepared samples exhibit a typical diffraction peak at 27.2° (Figures S14–S16), indexed to the g-C_3N_4 as reported previously.[3d,9] This suggests that the present strategy maintains the intrinsic structure of g-C_3N_4 after phosphatizing treatment at 400 °C, which is an important advance in avoiding high temperature for making single-atom catalysts.[2e,10] The decrease in the intensity of the diffraction peak at 27.2° is attributed to the formation of defects in the g-C_3N_4 layers due to the thermolysis of MNPs. This is in accordance with electron spin resonance (ESR) results, in which the MPSA-CN shows an enhanced G factor at 3482 relative to MNP-CN, attributed to the formation of numerous unsaturated atoms (Figures S17–S19). In addition, the bonding of MPSAs with g-C_3N_4 unavoidably introduces some new electronic states into the band structure of g-C_3N_4, which changes the light adsorption range of MPSA-CN as

reflected by the transformed Kubelka–Munk function of the UV/Vis diffuse reflectance spectra (DRS) (Figures S20–S22).

To explain the mechanism of the MNP-to-MPSA transformation on g-C_3N_4, we conducted density functional theory (DFT) calculations. Considering the numerous studies on the amorphization of crystals, here we mainly concentrated on the transformation of amorphous phosphatized metal NPs into MPSAs. In this process, PH_3 could assist the desorption of the metal atom by forming free M–xPH_3 (x = the number of PH_3 units) via the strong Lewis acid–base interaction between PH_3 and metal atoms.[8a] As shown in Figure 3a, when only one PH_3 unit was captured on one metal atom, the rate-determining formation of free M–PH_3 accounted for the energy barrier of 5.29 eV for Ru, 3.44 eV for Rh, and 1.53 eV for Pd, respectively. However, with two PH_3 units on one metal atom, the formation energy barrier of free M–$2PH_3$ decreased to 4.52 eV for Ru, 2.50 eV for Rh, and 0.53 eV for Pd, respectively (Figure 3b). Due to the geometric limitations, the adsorption of more than two PH_3 units on one metal atom was not supported by thermodynamics. However, the third PH_3 unit can assist the desorption of M–$2PH_3$ by forming free M–$3PH_3$, like the Volmer–Heyrovsky reaction (Figure 3c). Thus the smaller formation energy barrier of free M–$3PH_3$ was obtained on Ru (3.08 eV), Rh (1.28 eV), and Pd (−0.07 eV). However, it should be noted that Pd transfer from Pd–$3PH_3$ to g-C_3N_4 has a high reaction energy (1.24 eV). Hence, the pathways in Figure 3b for the formation of M–

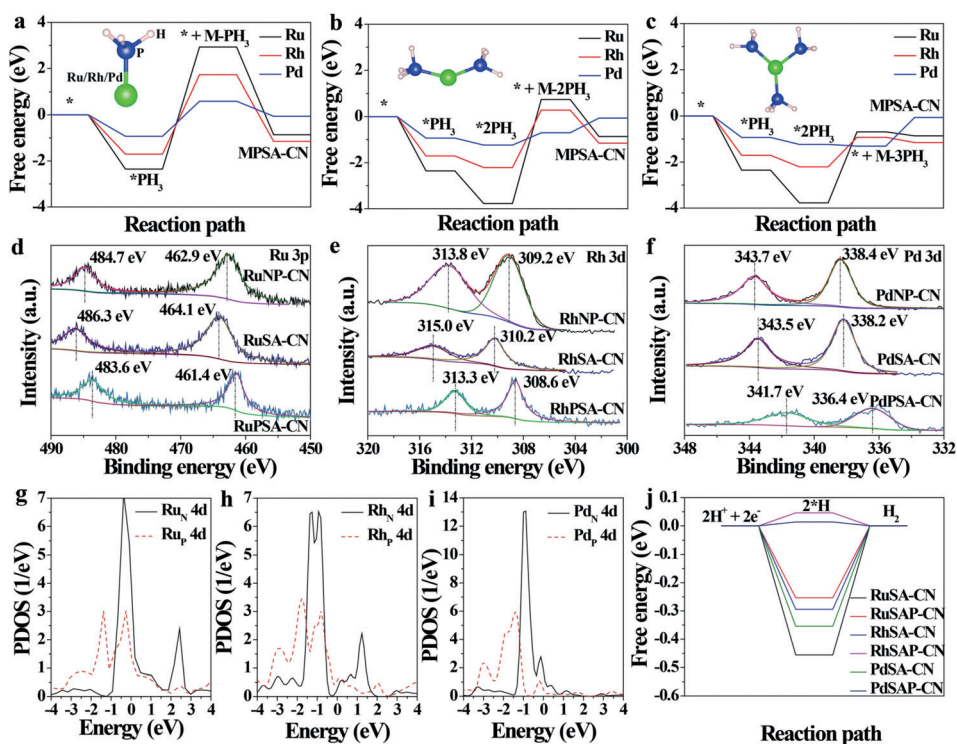**Figure 3.** The free energy of the system along the pathway of the transformation of MPNPs to MPSAs with a) M–PH_3, b) M–$2PH_3$, and c) M–$3PH_3$ as the intermediate state. High-resolution XPS of d) Ru 3p, e) Rh 3d, and f) Pd 3d. The PDOS plots of g) Ru_N 4d and Ru_P 4d, h) Rh_N 4d, and i) Rh_P 4d, g) Pd_N 4d and Pd_P 4d. j) The free energy diagram for the MSA-CN and MPSA-CN in HER. * stands for the solid surface. *PH_3 stands for the PH_3-adsorbed solid surface. Ru_N and Ru_P stand for the Ru atoms coordinated with N and P atoms, respectively.

2PH$_3$ and Figure 3c for the formation of M–3PH$_3$ correspond to the optimized formation of P-coordinated PdSAs and Ru/RhSAs from amorphous phosphatized metal NPs.

The above XANES results suggest that P coordination inhibits the oxidation of PdSAs. Here, the X-ray photoelectron spectroscopy (XPS) show the negative shift of Ru 3p, Rh 3d, and Pd 3d peaks in MPSA-CN compared to those in MNP-CN and MSA-CN, indicating more valence electrons in the MPSAs (Figure 3d–f). This result is consistent with the XANES spectra in Figure 1g and Figure S8. Besides, the XPS analysis on the surface C and N atoms of g-C$_3$N$_4$ indicates that the P coordination leads to a positive shift of the C 1s and N 1s peaks in MPSA-CN, implying the decrease of electrons on the g-C$_3$N$_4$ support (Figures S23–S25). These results reveal the electron transfer from the g-C$_3$N$_4$ to the MPSAs. In this process, the P ligands act as the electron-transfer channel between the g-C$_3$N$_4$ and the MPSAs. To verify the important role of P ligands in improving the electron density of the metal centers, DFT simulations were performed to investigate the electronic properties of N- and P-coordinated Ru, Rh, and Pd SAs on g-C$_3$N$_4$. The obtained projected density of states (PDOS) results show that the 3d states of N-coordinated MSAs are localized in a higher-energy region compared to those of P-coordinated MSAs (Figure 3g–i). In particular, most 3d states of MPSAs are localized below the Fermi level and are filled with electrons. However, the partially filled 3d states of N-coordinated MSAs are higher than the Fermi level and are electron-deficient. This further implies the electron-rich feature of the MPSAs.

For a given reduction reaction, the high electron density at the catalytic center is typically beneficial for electron transfer from the catalyst to the reactant molecules, contributing to the low formation barrier of products. Here, we used the hydrogen evolution reaction (HER) as the model reaction to investigate the relationship between the coordination environment and HER activity of MSAs. The results of DFT calculations show that the energy barrier of HER on MPSAs is obviously smaller than that on N-coordinated MSA (Figure 3j). In particular, the PdPSAs on g-C$_3$N$_4$ exhibit the lowest HER barrier of approximately zero. This difference between the HER activities of P- and N-coordinated MSAs can be explained by the fact that the higher electron density in the P-coordinated MSAs promotes the reduction of hydrogen.

Inspired by the above experimental results and theoretical speculation, we next investigated the catalytic activity of the as-prepared samples for H$_2$ evolution reaction (HER) under visible-light irradiation, which is an important process to convert solar energy into stored hydrogen energy. The experiment was performed in a Pyrex vessel under irradiation of a 300 W Xe lamp with a 420 nm cutoff filter, and using triethanolamine as the electron donor. The results show that MPSA-CN has higher photocatalytic H$_2$ production than MNP-CN or MSA-CN (Figure 4a). The H$_2$ production rate (1.98 mmol g^{-1} h^{-1}) of PdPSA-CN is 12 times higher than that of PdNP-CN, indicating the promotion effect of the MNP-to-MPSA transformation on improving the HER activity of Pd catalysts. Besides, the H$_2$ production rate of PdPSA-CN is also 4 times higher than that of the PdSA-CN, suggesting the
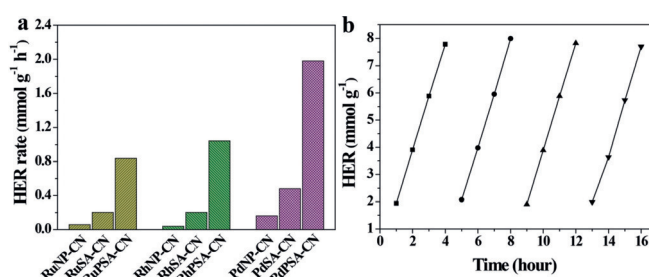

Figure 4. a) The H$_2$ production rates of different as-prepared samples and b) the cycled H$_2$ production activity of PdPSA-CN. All H$_2$ production experiments used triethanolamine as the sacrificial agent. The H$_2$ production rates were tested under visible-light (>420 nm) irradiation.

crucial role of phosphorus coordination in enhancing the HER activity of Pd single atoms. This result is in good agreement with the above theoretical speculations. Moreover, the stability test shows that PdPSA-CN can be used for 16 h without a decrease in activity (Figure 4b). The high stability of PdPSA-CN can be attributed to the strongly P-coordinated Pd single atoms. This clearly indicates the significance of the phosphorization-promoted MNP-to-MPSA transformation for improving the H$_2$-production activity in the photocatalytic reaction.

To summarize, we report a PH$_3$-assisted thermolysis strategy to synthesize a new class of the phosphorus-coordinated noble metal (Ru, Rh, Pd) single-atom catalysts on g-C$_3$N$_4$ nanosheets from noble metal nanoparticles at a low temperature of 400 °C. The obtained MPSAs show an exceptional electron-rich feature, which increases their H$_2$-production activity in the photocatalytic reaction. The present finding highlights a new low-temperature phosphorization strategy to prepare exceptionally active metal SAs on the catalyst surface for potential application in different catalytic fields.

Conflict of interest

The authors declare no conflict of interest.

[1] a) X. Z. Fang, Q. C. Shang, Y. Wang, L. Jiao, T. Yao, Y. F. Li, Q. Zhang, Y. Luo, H. L. Jiang, *Adv. Mater.* **2018**, *30*, 1705112; b) Z. G. Geng, Y. Liu, X. D. Kong, P. Li, K. Li, Z. Y. Liu, J. J. Du, M. Shu, R. Si, J. Zeng, *Adv. Mater.* **2018**, *30*, 1803498; c) X. G. Li, W. T. Bi, L. Zhang, S. Tao, W. S. Chu, Q. Zhang, Y. Luo, C. Z. Wu, Y. Xie, *Adv. Mater.* **2016**, *28*, 2427; d) J. D. Kistler, N. Chotigkrai, P. H. Xu, B. Enderle, P. Praserthdam, C. Y. Chen, N. D. Browning, B. C. Gates, *Angew. Chem. Int. Ed.* **2014**, *53*, 8904; *Angew. Chem.* **2014**, *126*, 9050; e) L. Z. Zhang, Y. Jia, G. P. Gao, X. C. Yan, N. Chen, J. Chen, M. T. Soo, B. Wood, D. J. Yang, A. J. Du, X. D. Yao, *Chem* **2018**, *4*, 285; f) H. G. Zhang, S. Hwang, M. Y. Wang, Z. X. Feng, S. Karakalos, L. L. Luo, Z. Qiao, X. H. Xie, C. M. Wang, D. Su, Y. Y. Shao, G. Wu, *J. Am. Chem. Soc.* **2017**, *139*, 14143; g) J. J. Shan, M. W. Li, L. F. Allard, S. S. Lee, M. Flytzani-Stephanopoulos, *Nature* **2017**, *551*, 605.

[2] a) H. F. Xiong, S. Lin, J. Goetze, P. Pletcher, H. Guo, L. Kovarik, K. Artyushkova, B. M. Weckhuysen, A. K. Datye, *Angew. Chem. Int. Ed.* **2017**, *56*, 8986; *Angew. Chem.* **2017**, *129*, 9114; b) A. Datye, Y. Wang, *Natl. Sci. Rev.* **2018**, *5*, 630–632; c) G. D. Sun, Z. J. Zhao, R. T. Mu, S. J. Zha, L. L. Li, S. Chen, K. T. Zang, J. Luo, Z. L. Li, S. C. Purdy, A. J. Kropf, J. T. Miller, L. Zeng, J. L. Gong, *Nat. Commun.* **2018**, *9*, 4454; d) Z. L. Zhang, Y. H. Zhu, H. Asakura, B. Zhang, J. G. Zhang, M. X. Zhou, Y. Han, T. Tanaka, A. Q. Wang, T. Zhang, N. Yan, *Nat. Commun.* **2017**, *8*, 16100; e) J. Jones, H. F. Xiong, A. T. Delariva, E. J. Peterson, H. Pham, S. R. Challa, G. S. Qi, S. Oh, M. H. Wiebenga, X. I. P. Hernandez, Y. Wang, A. K. Datye, *Science* **2016**, *353*, 150.

[3] a) C. Z. Zhu, S. F. Fu, Q. R. Shi, D. Du, Y. H. Lin, *Angew. Chem. Int. Ed.* **2017**, *56*, 13944; *Angew. Chem.* **2017**, *129*, 14132; b) A. Aitbekova, L. H. Wu, C. J. Wrasman, A. Boubnov, A. S. Hoffman, E. D. Goodman, S. R. Bare, M. Cargnello, *J. Am. Chem. Soc.* **2018**, *140*, 13736; c) M. Moliner, J. E. Gabay, C. E. Kliewer, R. T. Carr, J. Guzman, G. L. Casty, P. Serna, A. Corma, *J. Am. Chem. Soc.* **2016**, *138*, 15743; d) P. Zhou, F. Lv, N. Li, Y. Zhang, Z. Mu, Y. Tang, J. Lai, Y. Chao, M. Luo, F. Lin, J. Zhou, D. Su, S. Guo, *Nano Energy* **2019**, *56*, 127; e) A. Q. Wang, J. Li, T. Zhang, *Nat. Rev. Chem.* **2018**, *2*, 65; f) R. X. Qin, P. X. Liu, G. Fu, N. F. Zheng, *Small Methods* **2018**, *2*, 1700286.

[4] a) X. Wang, W. Chen, L. Zhang, T. Yao, W. Liu, Y. Lin, H. Ju, J. Dong, L. Zheng, W. Yan, X. Zheng, Z. Li, X. Wang, J. Yang, D. He, Y. Wang, Z. Deng, Y. Wu, Y. Li, *J. Am. Chem. Soc.* **2017**, *139*, 9419; b) Y. Tang, Y. T. Li, V. Fung, D. E. Jiang, W. X. Huang, S. R. Zhang, Y. Iwasawa, T. Sakata, L. Nguyen, X. Y. Zhang, A. I. Frenkel, F. Tao, *Nat. Commun.* **2018**, *9*, 1231; c) Y. R. Xue, B. L. Huang, Y. P. Yi, Y. Guo, Z. C. Zuo, Y. J. Li, Z. Y. Jia, H. B. Liu, Y. L. Li, *Nat. Commun.* **2018**, *9*, 1460; d) P. X. Liu, Y. Zhao, R. X. Qin, S. G. Mo, G. X. Chen, L. Gu, D. M. Chevrier, P. Zhang, Q. Guo, D. D. Zang, B. H. Wu, G. Fu, N. F. Zheng, *Science* **2016**, *352*, 797.

[5] a) R. Jiang, L. Li, T. Sheng, G. F. Hu, Y. G. Chen, L. Y. Wang, *J. Am. Chem. Soc.* **2018**, *140*, 11594; b) W. G. Liu, L. L. Zhang, X. Liu, X. Y. Liu, X. F. Yang, S. Miao, W. T. Wang, A. Q. Wang, T. Zhang, *J. Am. Chem. Soc.* **2017**, *139*, 10790; c) J. Wang, Z. Q. Huang, W. Liu, C. R. Chang, H. L. Tang, Z. J. Li, W. X. Chen, C. J. Jia, T. Yao, S. Q. Wei, Y. Wu, Y. D. Lie, *J. Am. Chem. Soc.* **2017**, *139*, 17281; d) J. Zhang, X. Wu, W. C. Cheong, W. X. Chen, R. Lin, J. Li, L. R. Zheng, W. S. Yan, L. Gu, C. Chen, Q. Peng, D. S. Wang, Y. D. Li, *Nat. Commun.* **2018**, *9*, 1002; e) H. Li, L. Wang, Y. Dai, Z. Pu, Z. Lao, Y. Chen, M. Wang, X. Zheng, J. Zhu, W. Zhang, R. Si, C. Ma, J. Zeng, *Nat. Nanotechnol.* **2018**, *13*, 411; f) G. Vilé, D. Albani, M. Nachtegaal, Z. Chen, D. Dontsova, M. Antonietti, N. López, J. Pérez-Ramírez, *Angew. Chem. Int. Ed.* **2015**, *54*, 11265; *Angew. Chem.* **2015**, *127*, 11417.

[6] a) Y. J. Chen, S. F. Ji, W. M. Sun, W. X. Chen, J. C. Dong, J. F. Wen, J. Zhang, Z. Li, L. R. Zheng, C. Chen, Q. Peng, D. S. Wang, Y. D. Li, *J. Am. Chem. Soc.* **2018**, *140*, 7407; b) X. Zhou, Q. Shen, K. D. Yuan, W. S. Yang, Q. W. Chen, Z. H. Geng, J. L. Zhang, X. Shao, W. Chen, G. Q. Xu, X. M. Yang, K. Wu, *J. Am. Chem. Soc.* **2018**, *140*, 554; c) S. Büchele, Z. Chen, S. Mitchell, R. Hauert, F. Krumeich, J. Pérez-Ramírez, *ChemCatChem* **2019**, *11*, 2812.

[7] S. Back, J. Lim, N. Y. Kim, Y. H. Kim, Y. Jung, *Chem. Sci.* **2017**, *8*, 1090.

[8] a) Y. T. Qu, Z. J. Li, W. X. Chen, Y. Lin, T. W. Yuan, Z. K. Yang, C. M. Zhao, J. Wang, C. Zhao, X. Wang, F. Y. Zhou, Z. B. Zhuang, Y. Wu, Y. D. Li, *Nat. Catal.* **2018**, *1*, 781; b) S. Wei, A. Li, J. C. Liu, Z. Li, W. Chen, Y. Gong, Q. Zhang, W. C. Cheong, Y. Wang, L. Zheng, H. Xiao, C. Chen, D. Wang, Q. Peng, L. Gu, X. Han, J. Li, Y. Li, *Nat. Nanotechnol.* **2018**, *13*, 856.

[9] a) Y. Kang, Y. Yang, L. C. Yin, X. Kang, L. Wang, G. Liu, H. M. Cheng, *Adv. Mater.* **2016**, *28*, 6471; b) P. Zhou, J. Lai, Y. Tang, Y. Chao, F. Lin, S. Guo, *Appl. Catal. B* **2018**, *238*, 161.

[10] X. F. Yang, A. Q. Wang, B. T. Qiao, J. Li, J. Y. Liu, T. Zhang, *Acc. Chem. Res.* **2013**, *46*, 1740.